RESEARCH ARTICLE

NANO · MICRO small
www.small-journal.com

Sustainable Photocatalytic Acylation of Transition Metal Dichalcogenides with Atom Economy

*Ioanna K. Sideri, Ruben Canton-Vitoria, Hiram J. Ojeda-Galvan, Mildred Quintana, and Nikos Tagmatarchis**

Transition metal dichalcogenides (TMDs) are promising 2D nanomaterials for diverse applications, but their intrinsic chemical inertness hinders their modification. Herein, a novel approach is presented for the photocatalytic acylation of *2H*-MoS_2 and *2H*-$MoSe_2$, utilizing tetrabutyl ammonium decatungstate ($(nBu_4N)_4W_{10}O_{32}$) polyoxometalate complex as a catalyst and a conventional halogen lamp as a source of irradiation. By harnessing the semiconducting properties of TMDs, new avenues emerge for the functionalization of these materials. This novel photocatalytic protocol constitutes the first report on the chemical modification of 2D nanomaterials based on a catalytic protocol and applies to both aliphatic and aromatic substrates. The scope of the decatungstate-photocatalyzed acylation reaction of TMDs is explored by employing an alkyl and an aromatic aldehyde and the success of the methodology is confirmed by diverse spectroscopic, thermal, microscopy imaging, and redox techniques. This catalytic approach on modifying 2D nanomaterials introduces the principles of atom economy in a functionalization protocol for TMDs. It marks a transformative shift toward more sustainable and efficient methodologies in the realm of TMD modification and nanomaterial chemistry.

1. Introduction

In the quest for novel advanced 2D nanomaterials with tuned properties, several methodologies have been developed for the chemical modification of transition metal dichalcogenides (TMDs).[1] To fully exploit their intrinsic properties, modify them, or acquire new ones with the aim being to expand their applications, TMDs chemical modification is deemed absolutely necessary. However, TMDs are not inherently chemically reactive. On the one hand, chalcogens are locked in the crystalline structure by forming three covalent bonds with metal atoms. On the other hand, transition metals are "hidden" between two layers of chalcogens, making them stereochemically inaccessible. Various efforts have been made in this direction in order to activate and chemically modify TMDs, while the focus is centered on MoS_2 and its two common configurations, *1T* and *2H*.[2] One way to acquire reactivity derives from the exfoliation process followed for their top-down preparation. Particularly, ionic intercalation during liquid-phase exfoliation forces the transition of the thermodynamically favored *2H* phase to the *1T*, which showcases a much stronger nucleophilic character due to the presence of negative charges on its surface originating from ionic intercalation, thus allowing nucleophilic additions to take place on its reactive lattice.[3] On the contrary, exfoliated *2H*-TMDs although inherently inert, are also very well-explored in terms of their functionalization.[4] While these methodologies are all in analogy with basic organic transformations, up to now no catalytic methodology has ever been reported for the chemical modification of TMDs. At the same time, *2H*-TMDs are notorious semiconductors with valuable optoelectronic properties, unlike their antipode metallic phases *1T*.[5] These interesting qualities derive from the energy gap between the valence band and the conduction band, characteristic of semiconducting TMDs, and have been deployed accordingly for optoelectronic and transistor applications.[6] Simultaneously, the existence of a bandgap allows electrons to transition from the valence to the conduction band following appropriate excitation. This simple observation is a remarkable quality that has been at the forefront of studies on photoinduced processes taking place on the surface of TMDs. At the same time, the allowance of electronic transitions between two energy states upon photoexcitation that result in the generation of electron–hole pairs is also a basic principle of photocatalysis. Strikingly, this process has never been employed for TMDs own modification. The inherent

I. K. Sideri, R. Canton-Vitoria, N. Tagmatarchis
Theoretical and Physical Chemistry Institute
National Hellenic Research Foundation
48 Vassileos Constantinou Avenue, Athens 11635, Greece
E-mail: tagmatar@eie.gr
H. J. Ojeda-Galvan, M. Quintana
High Resolution Microscopy-CICSaB and Faculty of Science
Universidad Autonóma de San Luis Potosi
Av. Sierra Leona 550, Lomas de San Luis Potosi, SLP 78210, Mexico

The ORCID identification number(s) for the author(s) of this article can be found under https://doi.org/10.1002/smll.202311045

DOI: 10.1002/smll.202311045

band-gap energy of TMDs can actually be utilized as a powerful tool for their functionalization.

Decatungstate anion, often used as the tetrabutylammonium salt (TBADT, $(n\text{Bu}_4\text{N})_4[\text{W}_{10}\text{O}_{32}]$), has found widespread application in the framework of photocatalyzed synthesis, thanks to its unprecedented reactivity.[7] The role of the decatungstate anion as a photocatalyst was first reported back in the 1980s by Hill[8] and has thereafter been at the forefront of catalysis and photocatalysis for a series of organic transformations as a regenerable or effectively catalytic radical initiator.[9] Following its catalytic role in organic synthesis, decatungstate anion was later utilized for the chemical modification of nanomaterials, specifically for the direct photocatalytic acylation of C_{60}, a 0D carbon nanomaterial[10] and recently single-walled carbon nanotubes (SWCNTs) a 1D carbon nanomaterial, with the use of aldehydes.[11] In both cases, a new C—C bond is formed between the carbonyl's C atom of an aldehyde and a C atom of carbon nanomaterial's lattice. Decatungstate $W_{10}O_{32}^{-4}$ catalytic activity is attributed to the HOMO (Highest Occupied Molecular Orbital), which has an energy level as low as −7.13 eV and, once photoexcited, can therefore accept a H atom, through hydrogen atom transfer, from various functional groups, based on their hydrogen atom dissociation energy, yielding $W_{10}O_{32}^{-5}\bullet H^+$. Furthermore, the energy levels of the HOMO and LUMO (Lowest Unoccupied Molecular Orbital) of C_{60} (−5.87 and −4.18 eV, respectively)[12] are energetically intermediate between the energy levels of $W_{10}O_{32}^{-4}$ and $W_{10}O_{32}^{-5}\bullet H^+$ (−7.13 and −3.48 eV, respectively),[13] allowing for the transfer of an electron from $W_{10}O_{32}^{-5}\bullet H^+$ to C_{60}, creating the anionic radical $C_{60}\bullet^-$, which is the driving force of the reaction.[10] Similarly, for SWCNTs, the valence band and conduction band have appropriate interposed energies (−4.90 and −3.88 eV, respectively),[14] therefore a similar correlation with the energy levels of $W_{10}O_{32}^{-4}$ and $W_{10}O_{32}^{-5}\bullet H^+$ is achieved, effectively driving the reaction.[11]

Considering the aforementioned discussion and in an analogous fashion, the semiconducting properties of TMDs make them ideal candidates for the expansion of this methodology and transfer of this knowledge to 2D nanomaterials. This fact gives rise to the introduction of a catalytic methodology in the quiver of chemical transformations available for the modification of 2D nanomaterials in general. Catalytic methodologies are preferable compared to conventional ones since the formation of byproducts is successfully avoided, while the reaction rate is accelerated. The atom economy plays also a major role in such transformations. In detail, catalysis offers a notable advantage over conventional wet chemistry, by enabling precise control over reactions, leading to enhanced efficiency. Atom economy is a pivotal concept in this context, reflecting the proportion of reactant atoms that contribute to the desired product. Near-unity atom economy is the reactants and products' atomic balance, where all atoms included in the reactants are present in the desired products, eliminating any by-products and aligning with the principles of green chemistry. By minimizing the production of unwanted byproducts, catalytic transformations underscore sustainability, making them environmentally responsible choices for the future of materials science and chemical engineering. However, these assets have yet to be incorporated in any methodology so far regarding the modification of 2D nanomaterials in general. Therefore, the use of $W_{10}O_{32}^{-4}$ as a photocatalyst for the chemical manipulation of TMDs opens an enormous window of possibilities for their functionalization, handling, and feature in a broad scope of applications. Based on the aforementioned concept and aspiration, we envisioned a protocol for the photocatalytic acylation of *2H*-MoS_2 and *2H*-$MoSe_2$ using aldehydes as functionality and $(n\text{-Bu}_4\text{N})_4\text{W}_{10}\text{O}_{32}$ as photocatalyst.

Regarding *2H*-MoS_2 and *2H*-$MoSe_2$, their bandgap energy, for both exfoliated monolayer materials and their precursors bulk MoS_2 and $MoSe_2$, is known and very well studied.[15] In particular, for exfoliated monolayered MoS_2, the valence band position was experimentally determined by photoelectron spectroscopy in air (PESA) to be at −5.7 eV, and while the Fermi level was estimated using XPS, the conduction band is positioned at −3.8 eV.[4b] However, the precise calculation of the exact energy of the valence and conduction bands in the case of exfoliated few-layered material remains a challenge for the research community and is strongly dependent on the layers number, strain engineering, chemical doping, intercalation, and substrate engineering among others.[15] In any case, the bandgap energy ranges from 1.09 eV for bulk $MoSe_2$ to 1.89 eV for monolayered *2H*-MoS_2 and is positioned within the aforementioned experimental findings of monolayered 2H-MoS_2, which lies within the corresponding HOMO-LUMO energy range of $W_{10}O_{32}^{-4}$ (3.65 eV).[16] Precisely, in the case of monolayered $MoSe_2$, the valence band is reported at −5.05 eV, while the conduction band is at ≈−3.50 eV based on photoemission electron microscopy (PEEM) assays with deep ultraviolet (DUV) illumination, confirming the above syllogism.[17] This fact allows suitable association between the energy levels of $W_{10}O_{32}^{-4}$ and $W_{10}O_{32}^{-5}\bullet H^+$ and those of valence and conduction band of exfoliated TMDs, therefore it is energetically favored for a photocatalytic radical transformation to take place. In the present manuscript, we, for the first time, describe the photocatalytic acylation of MoS_2 and $MoSe_2$, giving rise to the debut of catalysis, in general, on the surface of 2D nanomaterials, aiming their modification through an environmentally friendly, sustainable, and easy-handling way with overall atom economy.

2. Results and Discussion

2.1. Photocatalytic Protocol

Initially, liquid-phase exfoliation of commercially available TMDs took place, with the aid of chlorosulfonic acid[18] to obtain exfoliated *2H*-MoS_2 and *2H*-$MoSe_2$. The aldehyde of choice for the study of the reaction was octanal, an aliphatic aldehyde, and exfoliated *2H*-MoS_2 was used as a representative of the TMD family. The best solvent employed for the reaction was a mixture of acetonitrile and dichlorobenzene in a 1:1 v/v ratio, while also inert conditions were deemed necessary. A conventional 500 W linear halogen lamp was usd as a light source and was carefully positioned 10 cm away, to avoid overheating of the reaction mixture. The parameters chosen for the formation of functionalized nanomaterial **1a** are depicted in **Figure 1** (top panel). The duration of the reaction was monitored with the aid of infrared spectroscopy, by assessing IR spectra every hour from a portion of the reaction mixture, after filtration to remove the catalyst and unreacted aldehyde.

Figure S1a (Supporting Information), depicts the obtained IR spectra of the photocatalytic reaction between *2H*-MoS_2 and

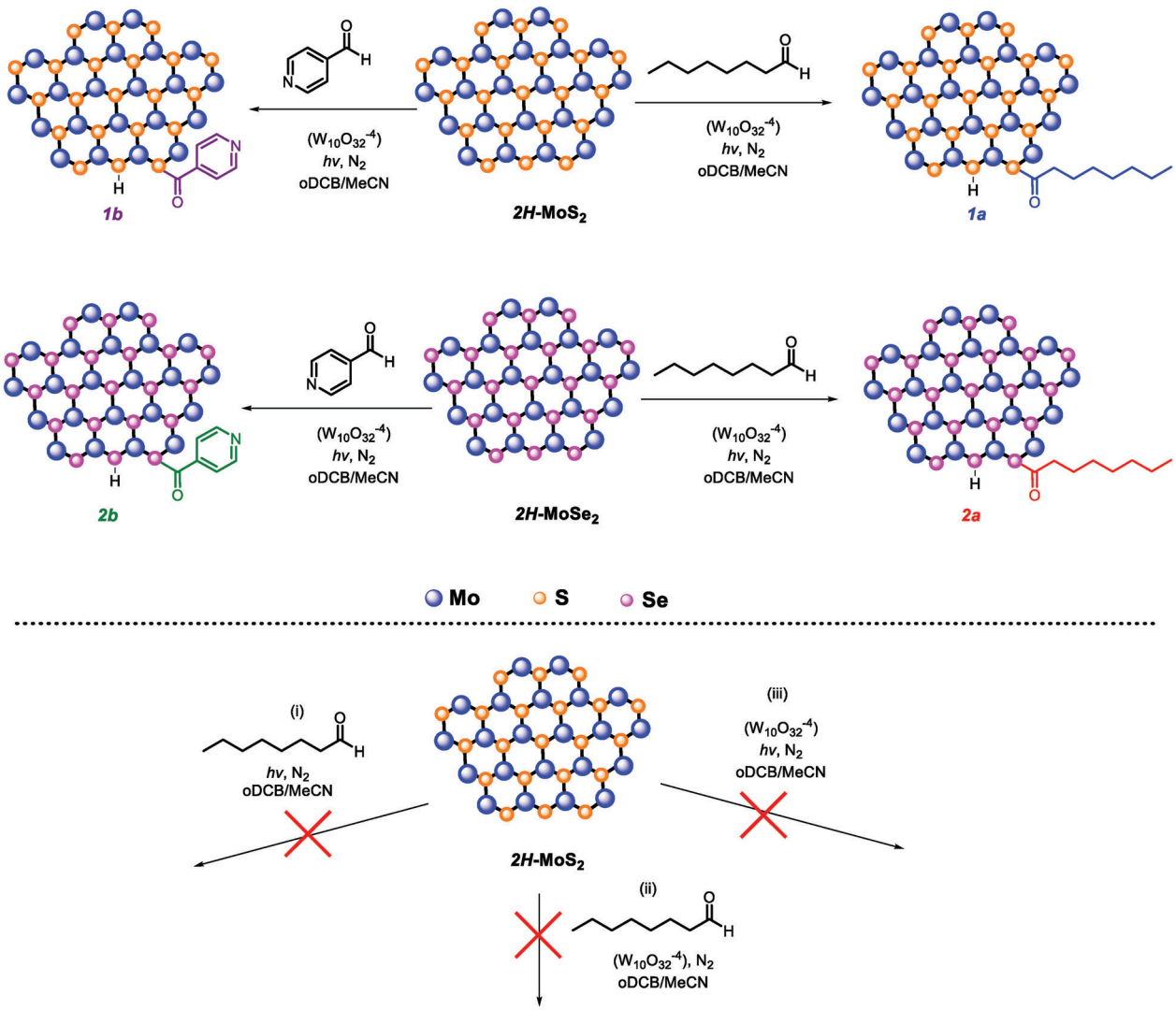

Figure 1. Top panel: Decatungstate-photocatalyzed acylation of *2H*-MoS_2 and *2H*-$MoSe_2$ with aromatic and aliphatic aldehydes. Bottom panel: blank experiments performed in the absence of i) TBADT, ii) light irradiation, and iii) octanal.

octanal in the presence of TBADT, recorded every hour over a span of 5 h, in comparison to the IR spectrum of exfoliated *2H*-MoS_2. It is evident that after only 1 h of irradiation, an absorption band at ≈1737 cm^{-1} already appears, which intensifies as the irradiation time progresses (Figure S1a, Supporting Information). By the 3-h mark, a distinct absorption band at 1737 cm^{-1}, attributed to the carbonyl stretching has clearly developed and remains intact after 5 h. Simultaneously, the stretching vibrations of aliphatic C—H bonds absorb in the range of 2980–2800 cm^{-1} and are already noticeable after 1 h. At 717 cm^{-1}, a weak absorption band is evident, attributed to the stretching vibration of the newly formed S—C bond. The aforementioned strong spectroscopic indications imply the formation of material **1a**. Variations of the reaction conditions were then conducted in order to investigate the role of each parameter regarding the success of the chemical transformation, using IR spectroscopy as a diagnostic tool. In Figure 1, bottom panel, the different reaction conditions tested, are depicted, which include: i) absence of the $(n\text{-}Bu_4N)_4W_{10}O_{32}$ catalyst, ii) absence of irradiation source, and iii) absence of the aldehyde. The IR spectra in the case of the variant conditions are presented in Figure S1b (Supporting Information). For comparison purposes, the IR spectrum of octanal and the reaction with the original parameters after 5 h of irradiation time, are provided. A simple observation of Figure S1b (Supporting Information) leads to the conclusion that the characteristic absorption band of the carbonyl stretching appears only in the IR spectrum of the original reaction conditions, with the simultaneous presence of $(n\text{-}Bu_4N)_4W_{10}O_{32}$ catalyst, light irradiation, and octanal, as well as the weak absorption of the S—C bond at 717 cm^{-1}. It is therefore reasonable to deduce that $(n\text{-}Bu_4N)_4W_{10}O_{32}$, octanal, and light irradiation are all essential parameters for the successful modification of *2H*-MoS_2 toward MoS_2-based functionalized material **1a**.

Having determined the preferred conditions for the catalytic reaction protocol, its applicability was tested in terms of organic substrates, where both aromatic and aliphatic aldehydes were

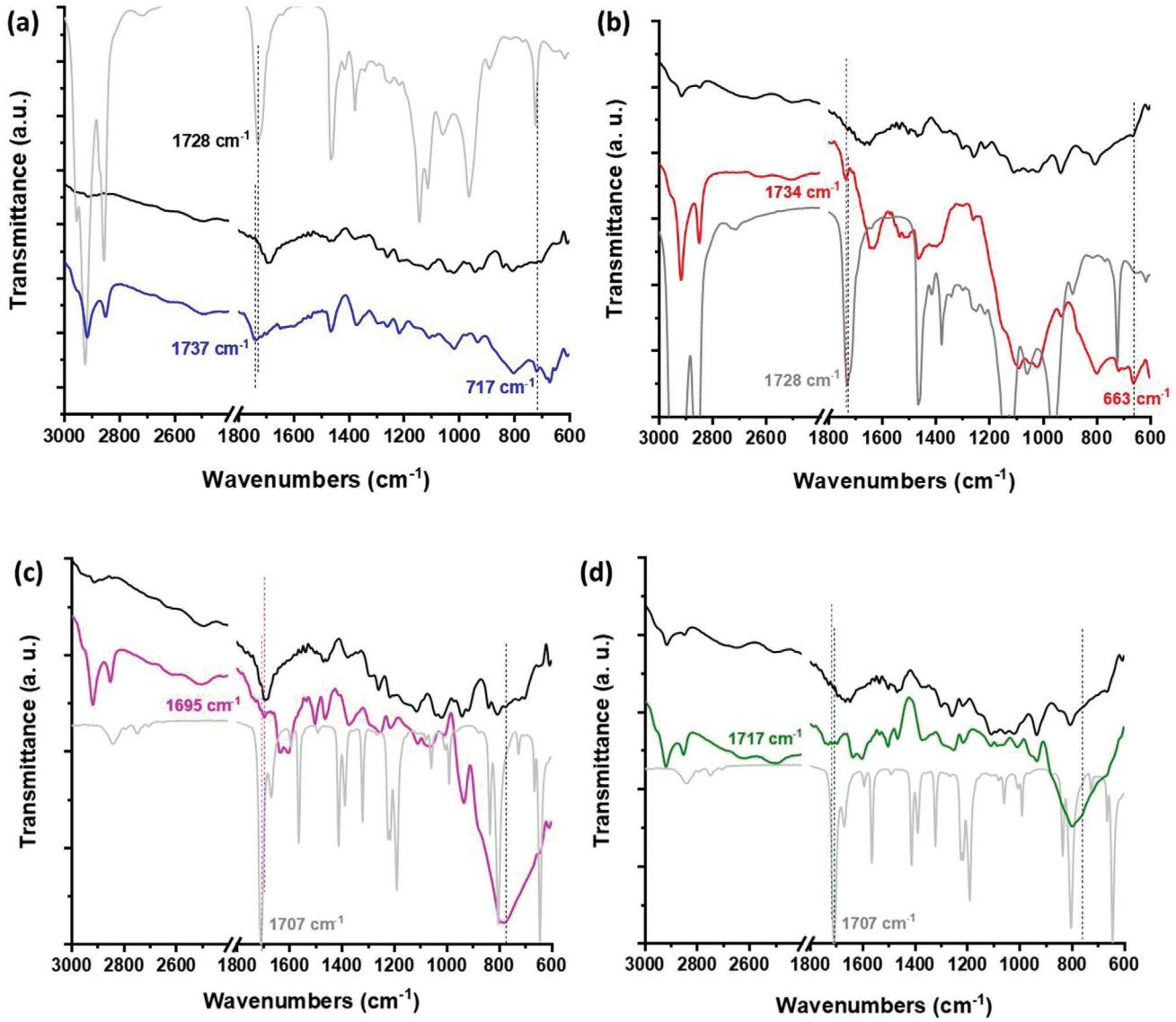

Figure 2. IR spectra of a) *2H*-MoS_2 (black), octanal (grey) and **1a** (blue), b) *2H*-$MoSe_2$ (black), octanal (grey) and **2a** (red), c) *2H*-MoS_2 (black), pyridine-4-carboxaldehyde (grey) and **1b** (pink) and d) *2H*-$MoSe_2$ (black), pyridine-4-carboxaldehyde (grey) and **2b** (green).

employed, as well as in terms of versatility in other 2D TMDs, specifically *2H*-$MoSe_2$. As an example of an aromatic aldehyde, pyridine-4-carbaldehyde was chosen, as its pyridine moiety offers further modification possibilities through coordination to metals as parts of chromophore units, such as porphyrins, phthalocyanines, etc. Figure 1 (top panel) also presents the materials synthesized using this particular methodology, which is noted as **1a**, **1b**, **2a**, and **2b**.

2.2. Characterization

2.2.1. IR Spectroscopy

IR spectroscopy constitutes the first tool for 2D TMDs characterization. **Figure** 2a presents the IR spectrum of **1a** in comparison with the corresponding spectrum of the precursor exfoliated *2H*-MoS_2 and octanal. Regarding functionalized material **1a**, as discussed previously, the diagnostic mode lies at 1737 cm^{-1} and corresponds to the stretching vibration of the carbonyl group, which can be roughly referred to as a thioester moiety. It is worth noting that there is a shift to higher wavenumbers compared to the respective band of the carbonyl stretching vibration of octanal, which is positioned at 1728 cm^{-1}. The same pattern is observed for the selenium-based aliphatic analog, **2a**. Focusing on the IR spectrum of **2a** in comparison with the corresponding spectrum of octanal, we observe a 6 cm^{-1} shift to higher wavenumbers of the band corresponding to the carbonyl stretching vibration of the selenoester moiety (Figure 2b).

The shift to higher frequencies of the carbonyl absorption band registered in both materials after the chemical reaction indicates covalent functionalization. The observed shift in higher

energy, which is observed upon formation of the C—S (and C—Se) bond on the TMD lattice, contradicts the situation on a molecular level, meaning that the carbonyl stretching vibration of an aliphatic thioester (and selenoester) generally absorbs in lower energy than the carbonyl of an aliphatic aldehyde. However, in the case of **1a** and **2a**, S atoms (or Se) connected to the carbonyl are parts of an extended lattice of metals and chalcogens, thus depriving vibrational degree(s) of freedom. Additionally, in modified material **2a**, the absorption of the stretching vibration of the C—Se bond which appears at 663 cm^{-1}, further validates the covalent attachment. Moving on to the corresponding IR spectra of materials **1b** and **2b**, which are modified with an aromatic aldehyde, we observe a different pattern. The carbonyl stretching vibration in **1b** (1695 cm^{-1}) appears at lower wavenumbers, compared to that of pyridine-4-carbaldehyde (1707 cm^{-1}), as shown in Figure 2c. Simultaneously, for material **2b**, the respective band is observed at 1717 cm^{-1} (Figure 2d). It is worth noticing that the carbonyl stretching vibration of the aromatic thioester absorbs at lower wavenumbers than the one of the aliphatic thioesters, which is also the case for modified materials **1a** and **1b**, respectively, owing to the electron-withdrawing effect of pyridine. Similarly, the aromatic selenoester absorbs at lower frequencies compared to the aliphatic one, which is also true for $MoSe_2$-based materials **2b** and **2a**, respectively. Overall, from the IR spectra, we can safely conclude that the catalytic acylation of MoS_2 and $MoSe_2$ is successful, furnishing the creation of new bonds C—S and C—Se in each case.

2.2.2. Raman Spectroscopy

Complementary, Raman spectroscopy is also used as a diagnostic tool to evaluate the success of the catalytic transformation. The characteristic in-plane transition E^1_{2g} (375 cm^{-1}), out-of-plane transition A_{1g} (405 cm^{-1}), and defect-induced 2LA(M) (450 cm^{-1}) modes, representing the crystalline lattice of MoS_2,[19] are evident in the respective Raman spectra of *2H*-MoS_2, **1a**, and **1b** (**Figure 3**). In this particular case, the acylation of MoS_2, as occurred via the formation of C—S bonds between the carbonyl carbon of aldehydes and the sulfur atoms of the MoS_2 lattice, constitutes the diagnostic evidence of the success of the catalytic reaction protocol. According to the rationale that the creation of new C—S bonds on the lattice surface generates electronic asymmetry and thus local strain at the positions of organic substituent binding and around them,[20] monitoring the intensity of the 2LA(M) band, that is directly related to lattice defects, is particularly important. In Figure 3a, which presents the average of multiple spectra for each material (normalized to the A_{1g} band), an increase in the intensity of the 2LA(M) band after chemical modification, is registered. Specifically, the variation in the intensity of the 2LA(M) band is represented both spatially and via the ratio of the intensities $I_{A1g}/I_{2LA(M)}$ in the Raman mapping areas of 30 μm × 30 μm in Figure 3b–d. For exfoliated *2H*-MoS_2, the $I_{A1g}/I_{2LA(M)}$ ratio is calculated as 0.99, while after the catalytic chemical modification, this ratio decreases to 0.77 for **1a** and to 0.81 for **1b**, confirming the electronic anisotropy induced to the sulfur atoms, that engage in the new covalent bonds, as well as their neighboring atoms that are also topologically affected by the change in the crystallinity of the lattice. Furthermore, the absence of the characteristic J_1, J_2, and J_3 Raman bands linked to the metallic *1T* phase of MoS_2, in the Raman spectra of the functionalized materials, confirms the dominant *2H* character of all three MoS_2-based materials. Overall, Raman spectroscopy reveals that no change is observed in terms of the semiconducting properties of the material upon functionalization.

However, regarding *2H*-$MoSe_2$ and its corresponding modified materials **2a** and **2b**, assessing their Raman spectra and linking them to covalent chemical modification is a challenging task. On the one hand, *2H*-$MoSe_2$ has not been extensively studied concerning its covalent modification, while on the other hand, *2H*-$MoSe_2$ appears to exhibit slight differences in its Raman fingerprint compared to other members of the TMD family.[21] In Figure S2 (Supporting Information), the average of multiple Raman spectra (633 and 785 nm) of $MoSe_2$-based materials *2H*-$MoSe_2$, **2a** and **2b** are presented, normalized to the A_{1g} mode, featuring the E_{1g} (139 cm^{-1}), out-of-plane transition A_{1g} (240 cm^{-1}), in-plane transition E^1_{2g} (281 cm^{-1}), and phonon mode 2LA(M) (311 cm^{-1}).[22] No significant changes are observed in either the intensity of the peaks or their relative positions. Considering that covalent modification of $MoSe_2$ has not been really described in the literature and spectroscopic Raman data are scarce, the 2LA(M) band may not be directly associated with any electronic asymmetry induced upon functionalization, as it is the case with MoS_2. For comparison purposes, the 2D Raman (633 nm) spectral mappings of the intensity ratio $I_{A1g}/I_{2LA(M)}$ of a 30 μm × 30 μm area of *2H*-$MoSe_2$, **2a** and **2b** are presented in Figure S2 (Supporting Information), where the absence of significant variation upon functionalization is further confirmed. In any case, the semiconducting nature of materials based on both MoS_2 and $MoSe_2$ is maintained after chemical modification, as evidenced by the Raman fingerprint of *2H* symmetry.

2.2.3. UV–Vis Spectroscopy

Following the aforementioned discussion regarding the presence of the semiconducting nature of the materials upon covalent functionalization, complementary UV–vis assays were conducted. In Figure S3 (Supporting Information), the UV–Vis spectra of *2H*-MoS_2, **1a**, **1b**, *2H*-$MoSe_2$, **2a** and **2b** are presented. In Figure S3a (Supporting Information), the excitonic bands A and B, which correspond to direct transitions from the K point of the Brillouin zone of the valence band to the conduction band, are evident in all three MoS_2-based materials.[23] These excitonic transitions are diagnostic of the semiconducting nature of the materials and a direct confirmation that no alterations on the semiconducting nature are registered upon covalent modification with the aldehydes of choice. On the basis of Figure S3b (Supporting Information), the same conclusion is drawn for the $MoSe_2$-based materials **2a** and **2b**. In particular, the absorbance band centered at 729 nm is attributed to the direct excitonic transition at the K-point in the Brillouin zone,[24] characteristic of the *2H* phase.

2.2.4. Thermogravimetric Analysis

The calculation of the degree of modification achieved through this specific photocatalytic methodology was the next goal of the

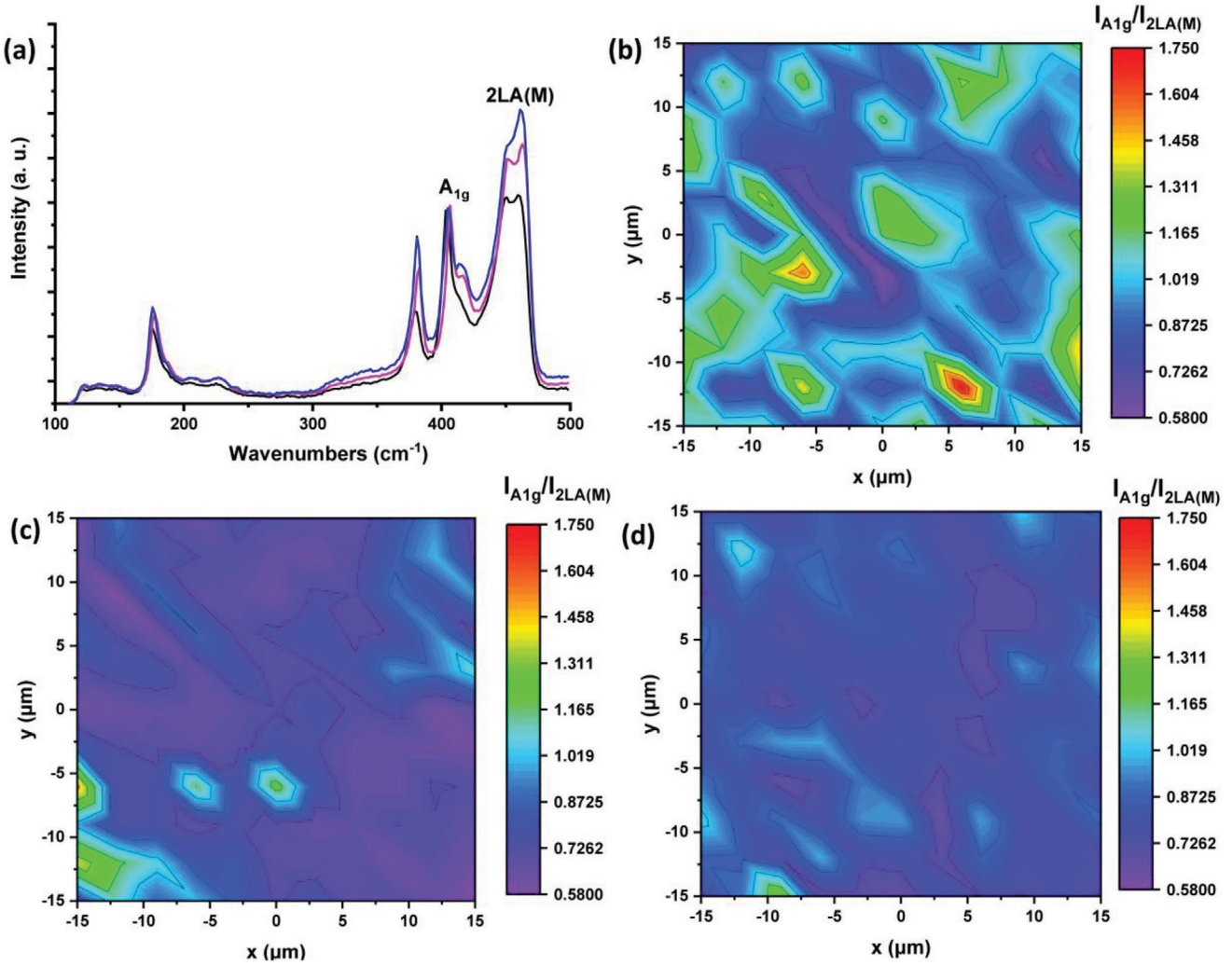

Figure 3. a) Average of multiple Raman spectra (633 nm) of MoS_2-based materials *2H*-MoS_2 (black), **1a** (blue), and **1b** (pink), normalized to the A_{1g} mode. 2D Raman spectral mapping of the intensity ratio $I_{A1g}/I_{2LA(M)}$ of a 30 μm × 30 μm area of b) *2H*-MoS_2, c) **1a**, and d) **1b**.

study. A useful tool in this endeavor constitutes the thermogravimetric analysis (TGA) technique. In **Figure 4**, TGA graphs of materials **1a**, **2a**, **1b**, and **2b**, are presented in comparison with those of the precursor exfoliated *2H*-MoS_2 and *2H*-$MoSe_2$. The dotted lines represent the second derivative of mass change with respect to the temperature change. While exfoliated *2H*-MoS_2 is relatively thermally stable up to 350 °C, within the same temperature range, a significant change for modified material **1a** is observed at 326 °C, corresponding to a mass loss of ≈5%, attributed to the thermal degradation of the organic substituent (Figure 4a). This mass loss translates to a 7% mol of organic substituent in modified material **1a**. On the other hand, *2H*-$MoSe_2$ is characterized by a thermal event at ≈330 °C, which is attributed to the thermal degradation of SeO_2 (sublimation point at 315 °C) due to the partial oxidation of $MoSe_2$ to MoO_3 and SeO_2 (Figure 4b).[25] This impurity handicaps the selective observation of the thermal event accounting for the degradation of the aliphatic substituent in **2a**. Still, in the TGA graph of **2a**, a clear mass change is observed at a lower temperature than the thermal degradation of SeO_2, at 279 °C, followed by a shoulder at 340 °C, which is probably associated with SeO_2 sublimation (Figure 4b). Approximately, it is estimated that there is a 1.5% mass loss attributed to the attachment of the aliphatic substituent, corresponding to a loading of 3% mol in material **2a**. Regarding the covalent modification with pyridine on *2H*-MoS_2, a 2% mass loss is recorded due to the thermal degradation of the aromatic substituent, corresponding to a 3% mol of organic substituent on material **1b** (Figure 4c). The corresponding mass loss attributed to covalent modification for material **2b** is 2.2%, corresponding to a degree of chemical modification of 5% mol (Figure 4d). The aforementioned molarity percentages (% mol) can be expressed also as a degree of functionalization in terms of organic units per MoX_2 unit. To do so, the molecular weight of a MoX_2 unit cell is taken into account and it is calculated that for **1a**, one organic chain is tethered every 14 MoS_2 units, while for **2a**, 1 octyl group is attached on the lattice every 31 $MoSe_2$ units. In an analogous manner, for **1b** and **2b**, the modification density is calculated as 1 organic moiety immobilized every 32 and 18 MoX_2 units, respectively. The same order

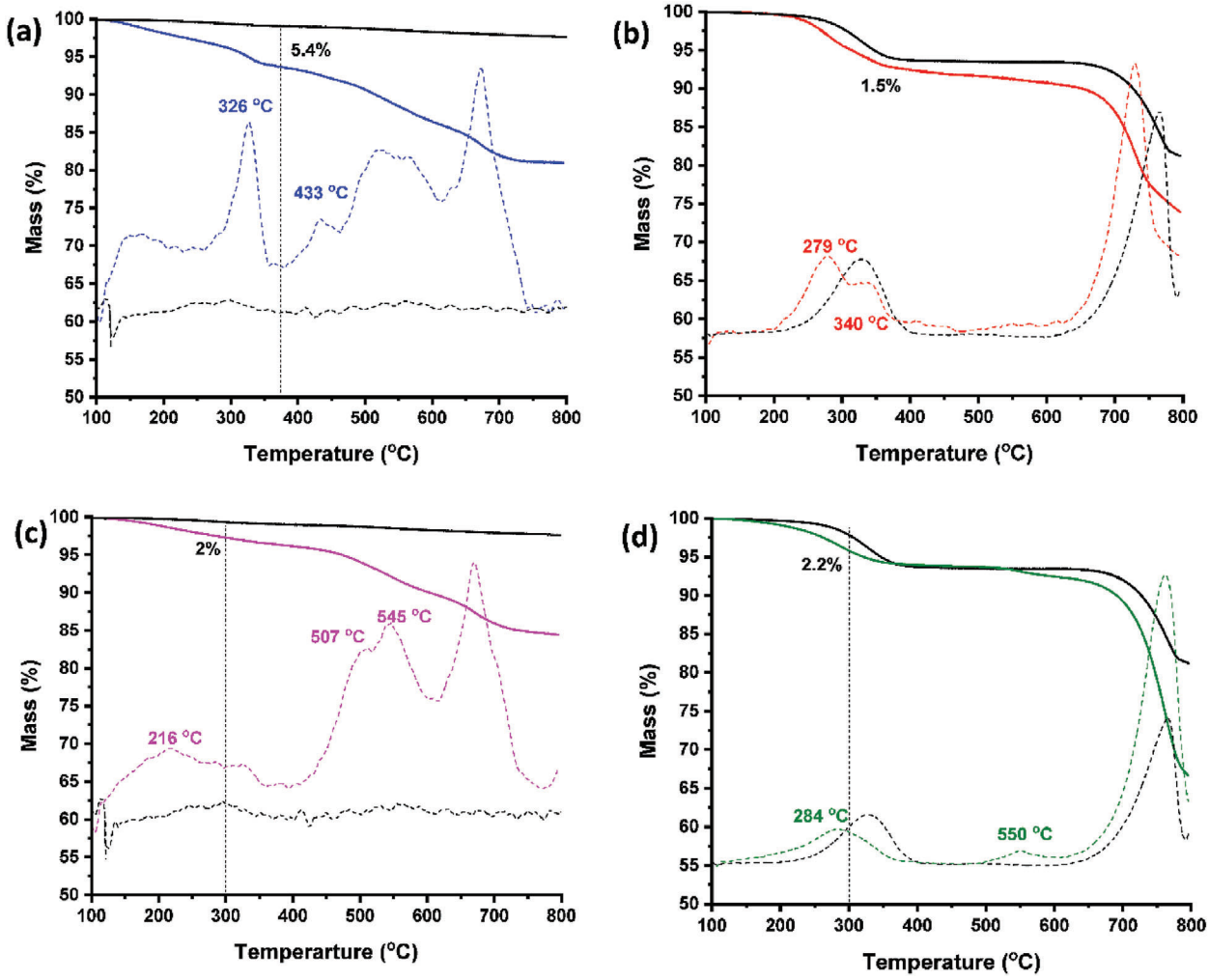

Figure 4. TGA graphs recorded under N_2 constant flow of a) *2H*-MoS_2 (black) and **1a** (blue), b) *2H*-$MoSe_2$ (black) and **2a** (red), c) *2H*-MoS_2 (black) and **1b** (pink) and d) *2H*-$MoSe_2$ (black) and **2b** (green). Dotted lines: second derivative curves of the mass change with respect to the temperature range for the respective entities.

of magnitude degree of chemical modification is registered for all materials, although no pattern is followed regarding the nature of the substituent (aliphatic vs aromatic). As far as *2H*-MoS_2 is concerned, a higher degree of modification is achieved with octanal than with pyridine-4-carbaldehyde. The exact opposite pattern is observed for *2H*-$MoSe_2$-based materials. In each case, the degree of chemical modification achieved is particularly high, considering the nature of the heterogeneous catalytic reaction.

2.2.5. Imaging

The morphological integrity of the photocatalytically obtained functionalized materials was evaluated by TEM and HR-TEM. Representative images exposing the characteristic (002) planes of each layered material were selected for their clear identification. In **Figure 5**, images of *2H*-MoS_2-based functionalized materials **1a**, **1b** and of *2H*-$MoSe_2$-based functionalized materials **2a**, **2b** are presented, in comparison with those of exfoliated *2H*-MoS_2 and *2H*-$MoSe_2$ (Figure 5a–d, respectively). A typical few layers *2H*-MoS_2 (Figure 5a) with totally straight edges and interplanar spacing of 0.62 nm is shown,[26] while for **1a** and **1b** (Figure 5b,c, respectively) materials with a small number of layers and disorderly edges are shown. Flawed edges with dislocations or terraces are clear indicators of covalent functionalization on the borders while the *2H*-MoS_2 plane is well preserved. Similarly, for exfoliated *2H*-$MoSe_2$ the characteristic interplanar spacing of 0.65 nm (Figure 5d) is shown.[27] Functionalized **2a** and **2b** materials are illustrated (Figure 5e,f, respectively), showing disordered and dislocated borders. Overall, the photocatalytic covalent functionalization results in exfoliated materials with a smaller number of layers as observed in Figure 5b–f.

2.2.6. Differential Pulse Voltammetry

Differential pulse voltammetry (DPV) was employed to shed light on the electronic structure of the materials. Initially, exfoliated

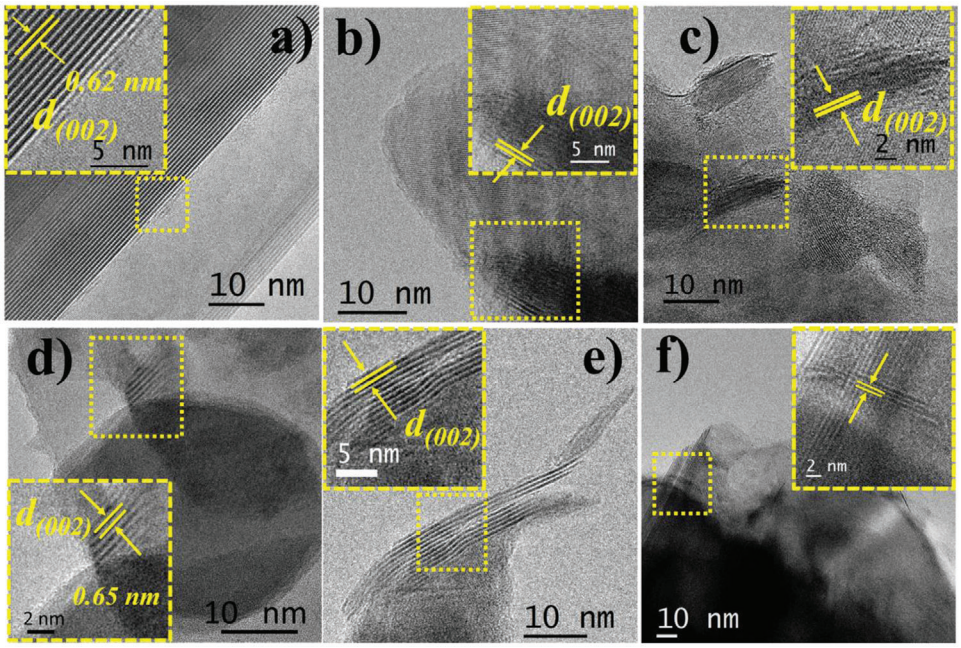

Figure 5. TEM and HR-TEM micrographs of photocatalytically modified materials. TEM image of a) exfoliated *2H*-MoS_2, b) **1a**, c) **1b**, d) exfoliated 2H-$MoSe_2$, e) **2a**, and f) **2b**. Insets include the HR-TEM analysis for each material.

2H-MoS_2 and *2H*-$MoSe_2$ exhibited a reduction peak at −0.81 and −0.72 V and an oxidation peak at 1.13 and 0.93 V versus NHE, respectively (**Figure 6**). Then, a bandgap of 1.94 and 1.65 eV was determined for *2H*-MoS_2 and *2H*-$MoSe_2$, respectively. Utilizing the ferrocene pair in the energy vacuum diagram (−4.8 eV), we derived the energies corresponding to the maximum valence band and minimum conduction band, resulting in −3.55 and −5.49 eV for MoS_2, and, −5.29 and −3.64 eV for $MoSe_2$, respectively. Although the energy levels can be influenced by various parameters, such as solvent, and production method of the TMDs (chemical vapor deposition versus liquid-phase exfoliation) potentially causing shifts of a few hundred meV, the redox potentials demonstrated consistency and alignment with the existing literature,[17] while being lower in energy than $W_{10}O_{32}^{-5}\bullet H^+$ (−3.48 eV), a key factor for driving the catalytic modification (see below for the mechanism). The additional oxidation peak observed at lower potentials for *2H*-MoS_2 and *2H*-$MoSe_2$, appearing at 0.98 and 0.73 V, respectively, is associated with defects at the edges of the TMDs, which are more reactive.[28,29] Turning to **1a**,**b** and **2a**,**b**, the reductive potentials persist without alteration. In contrast, the intensity of the oxidation redox potentials markedly decreases (Figure 6). A plausible explanation for this phenomenon is the utilization of electrons at the surface of MoS_2 and $MoSe_2$ to foster the formation of the new S—C and Se—C bonds, respectively. Furthermore, these electrons are potentially trapped in the newly created binding states, impeding the electrochemical oxidation process.

2.3. Mechanistic Insights

Having secured the success of the catalytic reaction protocol and the full characterization of the newly functionalized materials both spectroscopically and thermally, as well as structurally, the next goal was the unraveling of the mechanistic path followed. In principle, during a photocatalytic process, there are generally four certain steps taking place. Those include i) the light absorption in order to generate electron–hole pairs, ii) the separation of excited charges, iii) the recombination of those electrons and holes, and finally iv) the use of the active photocatalyst for the realization of the desired reaction.[30]

In the case of $W_{10}O_{32}^{-4}$, following photoexcitation, an electron from the 2p orbital of oxygen moves to the vacant 5d orbital of tungsten, leaving behind a hole in the oxygen, through charge transfer from the ligand to the metal. An excited state, that is $W_{10}O_{32}^{-4*}$, is populated, which is however considered chemically unreactive and decays to a reactive transient excited state form, noted in the literature as *w*O.[13] According to the literature, the latter is probably of triplet multiplicity, has a substantial charge transfer character,[31] and can therefore undergo a single electron transfer (SET) or hydrogen atom transfer (HAT) mechanism, leading to activation of the substrate by generating an active radical.[32] While in this case, the substrate is an aldehyde, which has been reported to form the acyl radical following a HAT pathway,[10,33] the SET pathway or the potential of some substrates under certain circumstances to react by both SET and HAT mechanisms, cannot be excluded.[32,34] Whether a HAT or a SET pathway takes place, the single-electron-reduced species of the decatungstate anion is formed after reduction, whether protonated $W_{10}O_{32}^{-5}\bullet H^+$ or not $W_{10}O_{32}^{-5}\bullet$.[34] In every case, a re-oxidation step is required to convert back the $W_{10}O_{32}^{-5}\bullet H^+$ or $W_{10}O_{32}^{-5}\bullet$ respectively to the $W_{10}O_{32}^{-4}$ un-reactive original species that is able to re-enter the catalytic cycle following photoexcitation. This oxidation occurs when an electron is transferred from $W_{10}O_{32}^{-5}\bullet H^+$ or $W_{10}O_{32}^{-5}\bullet$ to the TMD, which in turn is reduced to the $TMD^{\bullet-}$ radical anion. In our case,

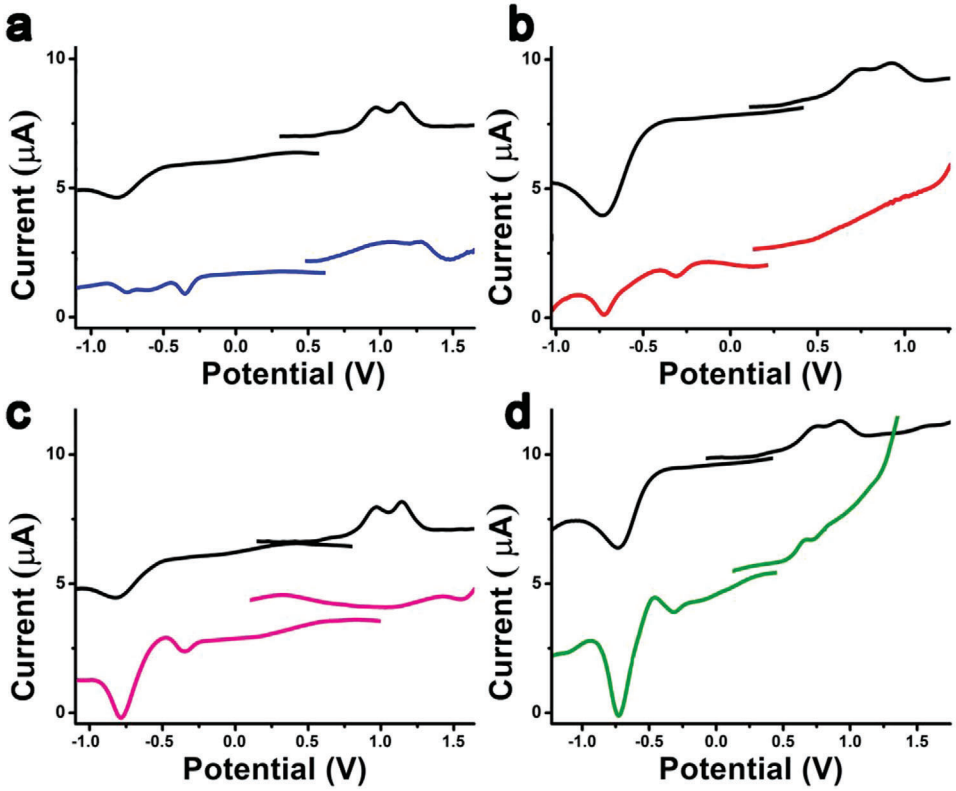

Figure 6. DPV of a) *2H*-MoS_2 (black), and **1a** (blue), b) *2H*-$MoSe_2$ (black), and **2a** (red), c) *2H*-MoS_2 (black), and **1b** (pink), and d) *2H*-$MoSe_2$ (black), and **2b** (green).

considering the aldehydes as the organic substrate, an acyl radical is formed following the already described pathway, but the progress of the reaction is then dependent on the formation of a $TMD^{\bullet-}$ radical, meaning TMDs ability to accept an electron (e^-) from their chemical environment. It should be noted that both the catalyst (TBADT) and the substrate (TMD) can absorb light upon light irradiation. Taking into account that the conventional halogen lamp, which is employed for this protocol, emits light across a broad spectrum covering the whole visible region, as well as the absorbance spectra characteristics of the materials (Figure S3, Supporting Information), both entities are subjected to potential excitation. In detail, TBADT absorbs intensely in the range of 200–350 nm, while TMDs have a broad absorption across the whole UV–Vis spectrum. However, in the same region (200–350 nm) TMDs also have a strong absorption, while this amount of energy when absorbed is highly likely to induce valence-to-conduction-band electronic transitions. Regarding TMDs, when an electron (e^-) transitions from the valence band to the conduction band upon excitation, it leaves a hole (h^+) in the valence band, which is positively charged due to the absence of a negative charge. Subsequently, if it is energetically allowed, the h^+ hole can capture an e^- from its nearby environment, creating the corresponding $TMD^{\bullet-}$ radical. Afterward, this radical adds to the acyl radical, resulting in the covalent modification of the TMD (**Figure 7**).[35] Energy-wise, the energy levels of the valence and conduction band of *2H*-MoS_2 are −5.7 and −3.85 eV, respectively,[4b] while *2H*-$MoSe_2$ lie at −5.05 and −3.50 eV, respectively.[17] This is further supported by the DPV assays (cf. Figure S2, Supporting Information), described above, where the valence and conduction bands of *2H*-MoS_2 and *2H*-$MoSe_2$ lie within the energy levels of $W_{10}O_{32}^{-4}$ and $W_{10}O_{32}^{-5}\bullet H^+$. Considering the energy levels of $W_{10}O_{32}^{-4}$ and $W_{10}O_{32}^{-5}\bullet H^+$ (−7.13 and −3.48 eV, respectively),[13] it is favorable for an electron to be transferred from $W_{10}O_{32}^{-5}\bullet H^+$ to the valence band of TMD, giving rise to the $TMD^{\bullet-}$ radical. Radical

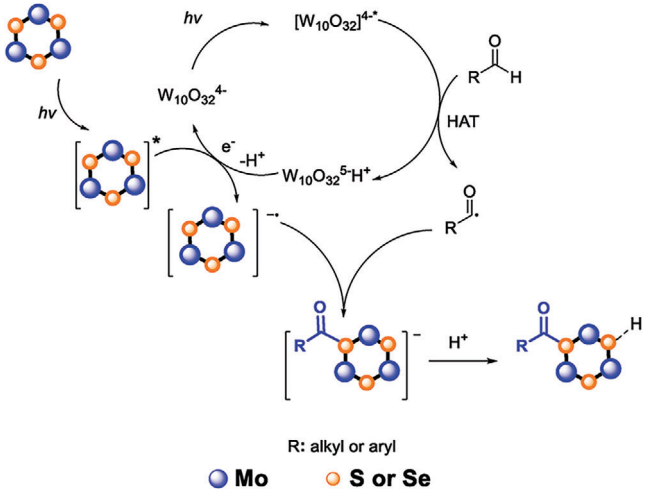

Figure 7. Proposed mechanism for photocatalytic acylation of *2H*-MoS_2 and *2H*-$MoSe_2$.

addition of the two generated radicals yields acylated TMD nanomaterials.

3. Conclusion

In summary, we have successfully demonstrated a groundbreaking photocatalytic approach for the acylation of *2H*-MoS_2 and *2H*-$MoSe_2$, utilizing $(n\text{Bu}_4\text{N})_4\text{W}_{10}\text{O}_{32}$ as a photocatalyst. This novel method capitalizes on the intrinsic semiconducting properties of TMDs, overcoming their chemical inertness and enabling covalent functionalization through a catalytic process. The chosen reaction conditions resulted in the formation of carbonyl groups and S—C (or Se—C) bonds on the TMD surfaces, unequivocally confirming successful modification. Raman and IR spectroscopy supported these findings as well as thermogravimetric analysis that further validated a high degree of chemical modification, underscoring the robustness of the catalytic approach. The successful introduction of this catalytic methodology opens up several promising future directions in TMDs research. First, extending the catalytic approach to other 2D materials and exploring the scope for functionalization with various aliphatic and aromatic aldehydes could further broaden the applicability of this efficient, atom-economical technique. Investigating the tunability of the catalytic reaction conditions to control the degree of modification and understanding the relationship between TMDs properties and the photocatalytic process are avenues for future exploration. The environmentally friendly and facile nature of our approach holds immense potential for an expanded field of applications, during an era where the demand for sustainable and efficient processes is on the rise.

4. Experimental Section

General Procedure Followed for the Photocatalytic Acylation of TMDs: In a round-bottom flask containing 5 mg of exfoliated *2H*-MoS_2 (or *2H*-$MoSe_2$, respectively), 5 mL of a mixture of solvents oDCB/MeCN (8.5/1.5) was added, along with 0.04 mol% $(Bu_4N)_4W_{10}O_{32}$ catalyst (0.15 µmol, 0.5 mg). The flask was then subjected to evacuation, filled with N_2, and evacuated again. This process is repeated for three consecutive cycles, with ultrasonic treatment of the reaction mixture for 5 min in between cycles. Finally, the flask was purged with N_2, and the respective aldehyde (0.4 mmol) was added using a syringe. The reaction mixture was placed in an ice bath under stirring and then irradiated using a conventional 500 W halogen lamp at a distance of 10 cm for 5 h. Subsequently, the reaction mixture was filtered through a PTFE filter and the solid material was washed with methanol, *N,N*-dimethylformamide, and dichloromethane. It was then dried under a high vacuum. Materials **1a**, **2a**, **1b**, and **2b** were isolated as a black powder, yielding ≈5 mg.

Supporting Information

Supporting Information is available from the Wiley Online Library or from the author.

Acknowledgements

This work was Financially supported by the Hellenic Foundation for Research and Innovation HFRI under the "2nd Call for HFRI Research Projects to support Faculty Members and Researchers," Project Number: 2482, is acknowledged.

Conflict of Interest

The authors declare no conflict of interest.

Data Availability Statement

The data that support the findings of this study are available from the corresponding author upon reasonable request.

Keywords

acylation, aldehydes, decatungstate, MoS_2, $MoSe_2$, photocatalysis

Received: December 20, 2023
Revised: January 3, 2024
Published online:

[1] A. Stergiou, N. Tagmatarchis, *Chem. - Eur. J.* **2018**, *69*, 18246.
[2] X. Chen, A. R. Mcdonald, *Adv. Mater.* **2016**, *28*, 5738.
[3] a) D. Voiry, A. Goswami, R. Kappera, C. D. C. C. E. Silva, D. Kaplan, T. Fujita, M. Chen, T. Asefa, M. Chhowalla, *Nat. Chem.* **2014**, *7*, 45; b) K. C. Knirsch, N. C. Berner, H. C. Nerl, C. S. Cucinotta, Z. Gholamvand, N. Mcevoy, Z. Wang, I. Abramovic, P. Vecera, M. Halik, S. Sanvito, G. S. Duesberg, V. Nicolosi, F. Hauke, A. Hirsch, J. N. Coleman, C. Backes, *ACS Nano* **2015**, *9*, 6018.
[4] a) Q. Ding, K. J. Czech, Y. Zhao, J. Zhai, R. J. Hamers, J. C. Wright, S. Jin, *ACS Appl. Mater. Interfaces* **2017**, *14*, 12734; b) E. P. Nguyen, B. J. Carey, J. Z. Ou, J. Van Embden, E. D. Gaspera, A. F. Chrimes, M. J. S. Spencer, S. Zhuiykov, K. Kalantar-Zadeh, T. Daeneke, *Adv. Mater* **2015**, *40*, 6225; c) M. Jeong, S. Kim, S.-Y. Ju, *RSC Adv.* **2016**, *43*, 36248.
[5] I. Song, C. Park, H. C. Choi, *RSC Adv.* **2014**, *5*, 7495.
[6] a) T. Mueller, E. Malic, *npj 2D Mater. Appl.* **2018**, *2*, 29; b) W. Choi, N. Choudhary, G. H. Han, J. Park, D. Akinwande, Y. H. Lee, *Mater. Today* **2017**, *3*, 116; c) C. Gong, Y. Zhang, W. Chen, J. Chu, T. Lei, J. Pu, L. Dai, C. Wu, Y. Cheng, T. Zhai, L. Li, J. Xiong, *Adv. Sci.* **2017**, *12*, 1700231.
[7] M. D. Tzirakis, I. N. Lykakis, M. Orfanopoulos, *Chem. Soc. Rev.* **2009**, *38*, 2609.
[8] C. L. Hill, *Synlett* **1995**, *1995*, 127.
[9] a) C. Tanielian, I. N. Lykakis, R. Seghrouchni, F. Cougnon, M. Orfanopoulos, *J. Mol. Catal. A: Chem.* **2007**, *262*, 170; b) D. Ravelli, M. Fagnoni, T. Fukuyama, T. Nishikawa, I. Ryu, *ACS Catal.* **2018**, *8*, 701; c) P. J. Sarver, V. Bacauanu, D. M. Schultz, D. A. Dirocco, Y.-H. Lam, E. C. Sherer, D. W. C. Macmillan, *Nat. Chem.* **2020**, *12*, 459; d) T. Varlet, D. Bouchet, E. Van Elslande, G. Masson, *Chem. - Eur. J.* **2022**, *56*, e202201707.
[10] M. D. Tzirakis, M. Orfanopoulos, *J. Am. Chem. Soc.* **2009**, *131*, 4063.
[11] R. Canton-Vitoria, M. Quintana, N. G. Malliaros, N. Tagmatarchis, *Adv. Mater. Interfaces* **2023**, *1*, 2201575.
[12] X. Zhang, X.-D. Li, *Chin. Chem. Lett.* **2014**, *25*, 501.
[13] V. D. Waele, O. Poizat, M. Fagnoni, A. Bagno, D. Ravelli, *ACS Catal.* **2016**, *6*, 7174.
[14] N. Murakami, Y. Tango, H. Miyake, T. Tajima, Y. Nishina, W. Kurashige, Y. Negishi, Y. Takaguchi, *Sci. Rep.* **2017**, *7*, 43445.
[15] A. Chaves, J. G. Azadani, H. Alsalman, D. R. Da Costa, R. Frisenda, A. J. Chaves, S. H. Song, Y. D. Kim, D. He, J. Zhou, A. Castellanos-Gomez, F. M. Peeters, Z. Liu, C. L. Hinkle, S.-H. Oh, P. D. Ye, S. J. Koester, Y. H. Lee, P. Avouris, X. Wang, T. Low, *npj 2D Mater. Appl.* **2020**, *4*, 29.
[16] a) A. Kumar, P. K. Ahluwalia, *Eur. Phys. J. B* **2012**, *85*, 186; b) K. K. Kam, B. A. Parkinson, *J. Phys. Chem.* **1982**, *86*, 463.

[17] K. Keyshar, M. Berg, X. Zhang, R. Vajtai, G. Gupta, C. K. Chan, T. E. Beechem, P. M. Ajayan, A. D. Mohite, T. Ohta, *ACS Nano* **2017**, *8*, 8223.
[18] G. Pagona, C. Bittencourt, R. Arenal, N. Tagmatarchis, *Chem. Commun.* **2015**, *51*, 12950.
[19] a) B. Chakraborty, H. S. S. R. Matte, A. K. Sood, C. N. R. Rao, *J. Raman Spectrosc.* **2013**, *1*, 92; b) S. Bae, N. Sugiyama, T. Matsuo, H. Raebiger, K.-I. Shudo, K. Ohno, *Phys. Rev. Appl.* **2017**, *7*, 024001. c) G. L. Frey, R. Tenne, M. J. Matthews, M. S. Dresselhaus, G. Dresselhaus, *Phys. Rev. B* **1999**, *60*, 2883.
[20] X. Chen, P. Denninger, T. Stimpel-Lindner, E. Spiecker, G. S. Duesberg, C. Backes, K. C. Knirsch, A. Hirsch, *Chem. - Eur. J.* **2020**, *29*, 6535.
[21] a) P. Soubelet, A. E. Bruchhausen, A. Fainstein, K. Nogajewski, C. Faugeras, *Phys. Rev. B* **2016**, *93*, 15; b) D. Nam, J.-U. Lee, H. Cheong, *Sci. Rep.* **2015**, *5*, 17113.
[22] X. Zhang, X.-F. Qiao, W. Shi, J.-B. Wu, D.-S. Jiang, P.-H. Tan, *Chem. Soc. Rev.* **2015**, *44*, 2757.
[23] L. Muscuso, S. Cravanzola, F. Cesano, D. Scarano, A. Zecchina, *J. Phys. Chem. C* **2015**, *119*, 3791.
[24] N. Dong, Y. Li, Y. Feng, S. Zhang, X. Zhang, C. Chang, J. Fan, L. Zhang, J. Wang, *Sci. Rep.* **2015**, *5*, 14646.
[25] C. Zheng, C. Chen, L. Chen, M. Wei, *J. Mater. Chem. A* **2017**, *37*, 19632.
[26] G. Deokar, D. Vignaud, R. Arenal, P. Louette, J.-F. Colomer, *Nanotechnology* **2016**, *27*, 075604.
[27] S. Masanta, C. Nayak, S. Maitra, S. Rudra, D. Chowdhury, S. Raha, M. Pradhan, B. Satpati, P. Pal, A. Singha, *ACS Appl. Nano Mater* **2023**, *6*, 5479.
[28] J. Bonde, P. G. Moses, T. F. Jaramillo, J. K. Nørskov, I. Chorkendorff, *Faraday Discuss.* **2009**,*140*, 219.
[29] S. J. Rowley-Neale, D. A. C. Brownson, G. C. Smith, D. A. G. Sawtell, P. J. Kelly, C. E. Banks, *Nanoscale* **2015**, *7*, 18152.
[30] S. Zhu, D. Wang, *Adv. Energy Mater.* **2017**, *33*, 1700841.
[31] D. C. Duncan, T. L. Netzel, C. L. Hill, *Inorg. Chem.* **1995**, *34*, 4640.
[32] I. Texier, J. A. Delaire, C. Giannotti, *Phys. Chem. Chem. Phys.* **2000**, *2*, 1205.
[33] S. Esposti, D. Dondi, M. Fagnoni, A. Albini, *Angew. Chem., Int. Ed.* **2007**, *46*, 2531.
[34] C. Tanielian, R. Seghrouchni, C. Schweitzer, *J. Phys. Chem. A* **2003**, *107*, 1102.
[35] P. P. Singh, S. Sinha, G. Pandey, V. Srivastava, *RSC Adv.* **2022**, *12*, 29826.